A computationally efficient thermo-mechanical model for wire arc additive manufacturing

Yang, Yabin; Zhou, Xin; Li, Quan; Ayas, Can

DOI
10.1016/j.addma.2021.102090

Publication date
2021

Document Version
Accepted author manuscript

Published in
Additive Manufacturing

Citation (APA)
Yang, Y., Zhou, X., Li, Q., & Ayas, C. (2021). A computationally efficient thermo-mechanical model for wire arc additive manufacturing. *Additive Manufacturing* , *46*, Article 102090. https://doi.org/10.1016/j.addma.2021.102090

A Computationally Efficient Thermo-mechanical Model for Wire Arc Additive Manufacturing

Yabin Yang[a,b,*], Xin Zhou[c], Quan Li[d], Can Ayas[e,*]

[a]*School of Materials Science and Engineering, Sun Yat-Sen University, Guangzhou, China*
[b]*Guangzhou Key Laboratory of Flexible Electronic Materials and Wearable Devices, Guangzhou, China*
[c]*Science and Technology on Plasma Dynamics Laboratory, Air Force Engineering University, Xi'an, China*
[d]*Capital Aerospace Machinery Corporation Limited, Beijing, China*
[e]*Department of Precision and Microsystems Engineering, Faculty of Mechanical, Maritime and Material Engineering, Delft University of Technology, Delft, the Netherlands*

Abstract

Residual stresses and distortions are major obstacles against the more widespread application of wire arc additive manufacturing. Since the steep temperature gradients due to a moving localised heat source are inevitable in this process, accurate prediction of the thermally induced residual stresses and distortions is of paramount importance. In the present study, a computationally efficient thermo-mechanical model based on a semi-analytical thermal approach incorporating Goldak heat sources is developed for the process modelling of wire arc additive manufacturing. The semi-analytical thermal model makes use of the superposition principle, and thereby decomposes the temperature field into an analytical temperature field to account for the heat sources in a semi-infinite space and a complementary temperature field to account for the boundary conditions. Since the steep temperature gradients are captured by the analytical solution, a coarse spatial discretisation can be used for the numerical solution of the complementary $\hat{T}$ field. Thermal evolution is coupled to an elasto-plastic mechanical boundary value problem that computes the thermal stresses and distortions. The accuracy of the proposed model is evaluated extensively by comparing the thermal and mechanical predictions with the corresponding experimental measurements as well as the simulation results obtained by a non-linear transient model from the literature. A thin wall structure with a length of 500 mm and consisting of 4 layers is modelled. The peak normal stress along the deposition direction can be predicted with less than 10% error. Furthermore, the simulations show that the part distortions are very sensitive to the boundary conditions.

Keywords: Wire arc additive manufacturing, thermo-mechanical modelling, computationally efficiency, Goldak heat source.

1. Introduction

Wire Arc Additive Manufacturing (WAAM) is a wire-based welding process, which has recently emerged as a prominent additive manufacturing technique to fabricate large metallic components. In WAAM, metallic material of choice is deposited in the form of beads at designated positions by melting a filler wire using electric arc as the heat source. The heat source path is controlled by a robotic arm to build 3D objects. WAAM is suitable for a wide range of materials, such as mild steel, titanium, and aluminium [1]. Compared to Laser Powder Bed Fusion (LPBF), the deposition rate of WAAM (2 – 10 kg/hour) is two orders of magnitude higher whereas the minimum feature size is also considerably bigger [2]. As a result, WAAM allows for the production of large scale products up to several meters.

Localised high energy input during the WAAM process leads to steep temperature gradients in the vicinity of the moving heat source. As a result, substantial levels of thermally induced residual stresses develop within the

*Corresponding author
Email addresses: yangyabin@sysu.edu.cn (Yabin Yang), c.ayas@tudelft.nl (Can Ayas)

component. Residual stresses lead to undesired distortions during subsequent machining operations and when cutting the part from the baseplate [3, 4]. Although residual stresses are unavoidable, proper process parameters and, a favourable deposition path can keep the residual stresses and the distortions below an acceptable level. Since it is expensive and time consuming to optimise process parameters and deposition path by experimental trial and error, modelling and simulation play a critical role for this purpose.

Numerical methods accounting for the complex, small-scale physical phenomena such as the melting of the electrode, droplet formation [5], fluid flow and heat transfer within the melt pool [6] are not feasible for modelling part-scale residual stresses and distortions due to the unacceptable computational costs associated. Finite element (FE) method, on the other hand, is by far the most widely used tool for this purpose. FE models analysing thermo-mechanical evolution combined with an element activation scheme to mimic the growing domain during the AM process are commonly used to predict the overall residual stresses and distortions, e.g. [7, 8]. In such FE models, phase transitions within the melt pool are usually neglected as a second-order effect [9]. For instance, FE modelling studies on WAAM presented by Zhao *et al.* [10] and Bai *et al.* [11] reported notable accuracy while neglecting the phase transitions.

The interaction between the heat source and the part being built can also be simplified by a distribution of heat flux with unit W/m^2 or power density with unit W/m^3. A 2D surface heat source, which assumes a Gaussian distribution of the heat flux, is first suggested by Pavelic *et al.* [12] and subsequently widely used in many studies, e.g. [13, 14]. However, this 2D surface source does not account for the depth of penetration of the heat source and, hence a 3D volumetric heat source is more realistic. Among the various 3D volumetric heat source models, the double semi-ellipsoidal heat source presented by Goldak *et al.* [15] is the most widely accepted one in simulating the welding based processes. Goldak source captures the steeper temperature gradients in front of the heat source compared to those at the trailing edge of the melt pool. Ding *et al*. [16] developed a thermo-mechanical model using Goldak heat source for simulating WAAM, and the predicted temperature histories, residual stresses and deformations agreed well with the experimental measurements [16].

However, a common problem for these FE models, including those for other metal additive manufacturing techniques, such as LPBF, is that the computational costs associated remain to be high. This is mainly due to the temporal and spatial mismatch between the heat source and the part inherent to AM [17, 18]. For WAAM, the heat source typically has a characteristic size on the order of several millimetres, while the dimension of the built part is on the order of meters. The total building time can be as long as several hours or days, while melt pool can cool down to room temperature within seconds to minutes. The above mentioned mismatch of time and length scales in the problem dictates a very fine spatial/temporal discretisation for a numerical solution of the heat equation thereby resulting in computationally intractable numerical models. In this regard, Ding *et al*. [16] developed a so-called "steady-state" thermo-mechanical model for WAAM aiming to improve the computational efficiency. In their "steady-state" model, the thermal problem is analysed with a single FE solve, based on the observation that a steady state of thermal history is usually attained in a long weld. Compared to its transient counterpart, the computational efficiency of the "steady-state" model is remarkably higher. However, this "steady-state" approach is limited to a long welding based process only. Ding *et al*. [16] justified the suitability of steady-state heat equation for a welding length of 500 mm. In a typical welding based additive manufacturing process, the welding path typically varies, e.g. the contour path or spiral path [19], and a steady-state of the thermal history may not be established. Therefore, a thermo-mechanical model which is capable of describing the WAAM process, not only limited to long welding, with notable accuracy and computational efficiency is a quintessential knowledge gap.

Yang *et al.* [20] developed a semi-analytical thermal approach and demonstrated that it is a computationally efficient and accurate scheme for thermal modelling of LPBF. In this approach, the moving heat source is discretised into many individual point heat sources. The closed-form analytical solution for each point heat source is known in a semi-infinite space. This analytical solution is then utilised to capture steep temperature gradients in the vicinity of the heat source. Boundary conditions (BCs) are enforced with a complimentary correction field, which is solved numerically. The key advantage of the semi-analytical approach is that the steep temperature gradients in the vicinity of a point heat source are captured by the analytical solution, independent of the spatial discretisation applied for the complementary correction field. Consequently, it is not necessary to use a very fine spatial discretisation to resolve the temperature fields associated with the point heat source. In contrast, an accurate solution can be obtained with relatively coarse mesh, which scales with the part dimensions, and the computational efficiency is significantly improved.

In LPBF, the part is produced in a layer-by-layer fashion along a fixed building direction orthogonal to the baseplate. However, in WAAM the building direction may vary during the process due to the capability provided by the robotic arm and the absence of loose powder covering the part. Hence in WAAM, the building direction is not necessarily fixed and thus not always orthogonal to the baseplate. Nevertheless, in practice, still, the most common way to build a component is in a layer-by-layer manner for a given building direction. In this paper, we adopt the semi-analytical approach to model the thermal evolution during the WAAM for a given building direction. We incorporate the Goldak heat source into the fully transient semi-analytical approach presented in [20] and further construct a computationally efficient thermo-mechanical model to calculate the residual stresses and deformations. Besides, in [20] the accuracy of the semi-analytical model was only validated by comparing the melt pool dimensions with the experiments in the literature. In the present paper, the accuracy of the proposed model is more directly evaluated by comparing the predicted temperature histories, stresses and distortions with the experiment performed by Ding *et al.* [16]. The computational cost of the proposed model is also reported.

The outline of the paper is as follows. Section 2 details the proposed superposition based semi-analytical model and explains how this model is applied for modelling the thermal histories of the WAAM process. The mechanical model is also briefly explained in this Section. In Section 3, the experiment conducted by Ding *et al.* [16], which is employed to validate the accuracy of the proposed model is detailed. The numerical parameters used in the proposed model are also carefully determined. In Section 4, the simulation results of the proposed model are summarised, and the accuracy of the proposed model is evaluated by comparing the predicted thermal histories, residual stresses and distortions with the corresponding experimental measurements. The article concludes with a reiteration of the most salient points of the study.

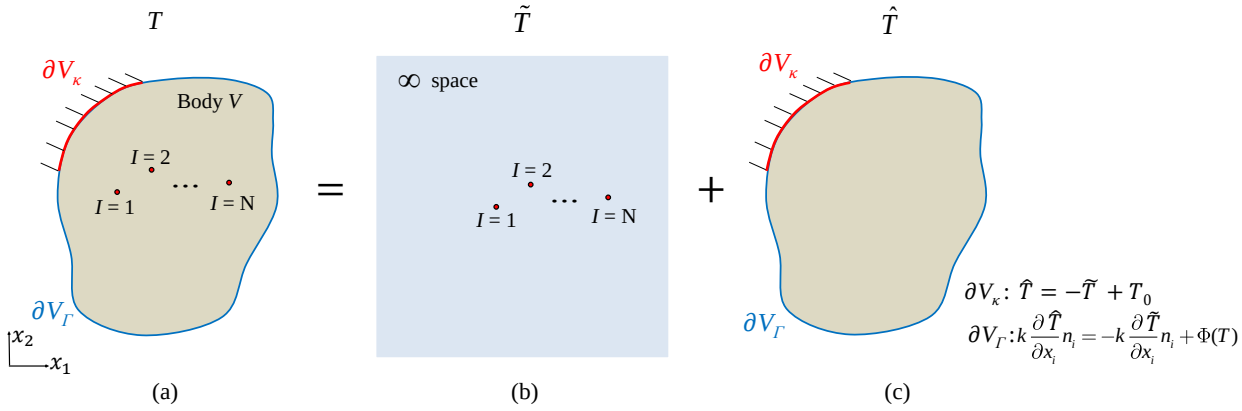

Figure 1: Schematic illustration of the superposition principle. (a) A continuum body containing N point heat sources is subject to Dirichlet BC on the boundary ∂V_κ and Neumann BC on the boundary ∂V_Γ. The temperature due to the N heat sources can be decomposed as the (b) temperature field $\tilde{T}$ due to N point heat sources in an infinite space and the (b) complementary correction field $\hat{T}$ to account for the BCs.

2. Model Description

WAAM process is a one-way coupled thermo-mechanical problem, which implies the effect of mechanical fields such as stress and strain on the temperature field is negligible. Therefore, for the proposed model, the thermal response is calculated first and used as an input to calculate the mechanical fields. In Section 2.1, the semi-analytical method for solving the heat equation based on the superposition principle is briefly presented. The semi-analytical approach employed for modelling WAAM is then described in Section 2.2. The mechanical model is briefly explained in Section 2.3.

2.1. Semi-analytical thermal approach

Consider the body V illustrated in Fig. 1a which contains N instantaneous point sources. Source I is activated at time instance $t = t_0^{(I)}$. The temperature response of body V to the N heat sources is governed by

$$\rho c_p \frac{\partial T}{\partial t} = \nabla \cdot (k \nabla T) + \dot{Q}, \tag{1}$$

where T is the temperature, $\dot{Q}$ is the rate of heat input, i.e. the source term. The material density, constant-pressure specific heat and conductivity are represented by ρ, c_p and k, respectively. If these thermal properties are considered as temperature independent constants, Eq. (1) becomes

$$\frac{\partial T}{\partial t} = \alpha \nabla^2 T + \frac{\dot{Q}}{\rho c_p}, \tag{2}$$

with the thermal diffusivity defined as $\alpha = k/\rho c_p$.

Now consider Dirichlet BC is enforced on some portion of the boundary ∂V_κ while Neumann BC is applied on the remaining boundary ∂V_Γ, as expressed by

$$T = T_0, \qquad \text{on} \quad \partial V_\kappa, \tag{3a}$$

$$k \frac{\partial T}{\partial x_i} n_i = \Phi(T), \quad \text{on} \quad \partial V_\Gamma, \tag{3b}$$

where T_0 is the prescribed temperature and $\Phi(T)$ is the prescribed heat flux which can be a function of temperature. The x_i component of the outward unit normal of ∂V_Γ is represented with n_i, where $i = 1, 2$ in 2D and $i = 1, 2, 3$ in 3D. The initial temperature $T(x_i, t = 0)$ is known represented with $T_{\text{ini}}(x_i)$.

Since Eq.(2) is linear, granted $\Phi(T)$ is a linear function of temperature T, and neglecting the phase transitions, the temperature field T can be obtained using the superposition principle [21, 22], which is given by

$$T = \tilde{T} + \hat{T}. \tag{4}$$

As illustrated in Fig. 1b, the $\tilde{T}$ field is the temperature field due to the $I = 1, 2, ..., N$ heat sources in the infinite space expressed as

$$\tilde{T}(x_i, t) = \sum_{I=1}^{N} \tilde{T}^{(I)}(x_i, t), \tag{5}$$

where $\tilde{T}^{(I)}$ is the temperature field due to heat source I in the infinite space. Since the closed form solution of $\tilde{T}^{(I)}$ is known, Eq. (5) can be calculated analytically.

The BCs associated with the finite dimensions of body V are accounted for with the complementary temperature field $\hat{T}$ (see Fig. 1c), which is governed by

$$\frac{\partial \hat{T}}{\partial t} = \alpha \nabla^2 \hat{T}, \tag{6}$$

with the BCs

$$\hat{T} = -\tilde{T} + T_0, \qquad \text{on} \quad \partial V_\kappa, \tag{7a}$$

$$k \frac{\partial \hat{T}}{\partial x_i} n_i = -k \frac{\partial \tilde{T}}{\partial x_i} n_i + \Phi(T), \quad \text{on} \quad \partial V_\Gamma. \tag{7b}$$

Eq. (7a) and Eq. (7b) are direct consequences of Eq. (3a) and Eq. (3b), respectively. The initial condition at $t = 0$ reads

$$\hat{T}(x_i, 0) = T_{\text{ini}}(x_i). \tag{8}$$

Provided $\tilde{T}$ and its gradient are finite on boundary surfaces ∂V, Eqs. (6 –8) define a smooth problem. Consequently, its numerical solution with FE requires the element size scaling with the dimensions of the body V.

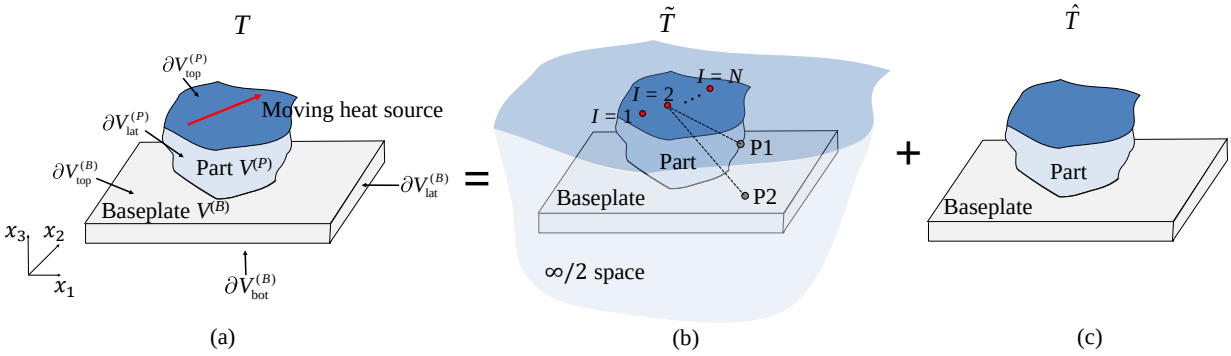

Figure 2: (a) A moving heat source is applied on the top surface $\partial V_{\text{top}}^{(P)}$ of the body V, which comprises the part $V^{(P)}$ and the baseplate $V^{(B)}$. The total temperature can be decomposed as the superposition of the (b) field $\tilde{T}$, which is the temperature due to a set of point heat sources in a semi-infinite space, and the (c) complementary field $\hat{T}$, which accounts for the BCs. In (b), the straight line from source $I = 2$ to point P1 is confined within body V, which satisfies the "convexity" requirement. However, the straight line from source $I = 2$ to point P2 violates the "convexity" requirement.

2.2. Thermal modelling of WAAM

It remains to utilise the semi-analytic approach to model the thermal evolution of a part during WAAM. For that purpose, we consider a 3D body V, which consists of the part $V^{(P)}$ and the baseplate $V^{(B)}$, as shown in Fig. 2a. The boundary surfaces of body V include the top and lateral surfaces of part $V^{(P)}$, denoted as $\partial V_{\text{top}}^{(P)}$ and $\partial V_{\text{lat}}^{(P)}$, respectively, and the top, lateral and bottom surfaces of the baseplate $V^{(B)}$, denoted as $\partial V_{\text{top}}^{(B)}$, $\partial V_{\text{lat}}^{(B)}$, and $\partial V_{\text{bot}}^{(B)}$, respectively. The baseplate and the part are assumed to have the same thermal properties. We assume the part is built in a layer-by-layer manner along a fixed building direction that coincides with the x_3 axis. Therefore, a moving heat source is introduced on the top surface $\partial V_{\text{top}}^{(P)}$ of the part.

Recall that in the semi-analytical approach, the governing equation, i.e. Eq. (2), is linear which requires the thermal material properties to be constant. Although for most materials the conductivity k and specific heat c_p are temperature dependent, it has been demonstrated that the temperature field predictions, as well as the melt pool dimensions can still be well-approximated with appropriate fixed values of k and c_p [20, 23, 24].

Radiation is neglected since the amount of heat lost due to radiation is negligible in comparison to the amount of heat transferred by conduction and convection. WAAM process takes place in open air, and a cooling system is usually employed to prevent heat accumulation. There are various cooling approaches used in WAAM, see e.g. [25] for details. Among these approaches, cooling the baseplate is one of the most convenient methods widely used in practice. This can be achieved for instance by means of placing a water cooling system underneath the baseplate (see e.g. [16]). Ding *et al.* [16] argued that the additional heat loss due to this cooling system can be modelled by increasing the value of the respective convection coefficient. Therefore, in the present model, convection BC is also applied to the bottom surface of the baseplate $\partial V_{\text{bot}}^{(B)}$ with a convection coefficient to mimic the cooling effect. For the other boundary surfaces, convection BC is also applied albeit with a smaller value of convection coefficient describing the heat transfer between the body and the surrounding atmosphere. Consequently, Neumann BCs are enforced on all boundary surfaces of body V, and the function $\Phi(T)$ appeared in Eq. (3b) is given by

$$\Phi(T) = h(T - T_\infty), \tag{9}$$

where h is the temperature independent convection coefficient to be determined for surfaces and T_∞ is the room temperature.

Phase transitions are not accounted for in the semi-analytical approach, despite melting takes place when the temperature exceeds the melting point T_m and vapourisation may occur with further temperature increase. This is because phase transitions introduce non-linearity in the governing equation and thus prohibit the use of the superposition

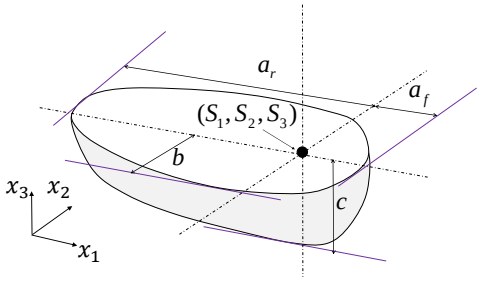

Figure 3: Schematic illustration of the geometry of a Goldak double semi-ellipsoidal heat source, which consists of the front semi-ellipsoid and the rear semi-ellipsoid. The centres of the two semi-ellipsoids are both S_i.

principle. It has been shown in [20, 23, 24] that considerable accuracy can be achieved while neglecting the phase transitions. The solid phase transformations are also neglected in the proposed model. These solid phase transformations seem to have an insignificant effect on the residual stresses for certain materials (such as mild steel) both for welding [26] and WAAM [16]. However, for some other materials (such as medium carbon steel [26]), the solid phase transformations might have a considerable effect on the residual stresses and distortions. Hence, the proposed model is suitable for the materials whose residual stresses and distortions are insensitive to the solid phase transformations in WAAM. As a result, with constant thermal properties, linear BCs and neglecting phase transformations, the thermal histories during WAAM are governed by the linear Eq. (2). Consequently, the semi-analytical approach based on the superposition principle is applied to the associated boundary value problem.

The decomposition of temperature T reminiscent to Fig. 1 is illustrated in Fig. 2. We consider the moving heat source as shown in Fig. 2a, which is discretised by a finite number of instantaneous heat sources (see Fig. 1b). Heat source I, where $I = 1, 2, ..., N$, is activated at the moment $t_0^{(I)}$ and the subsequent heat source $I + 1$ is activated at the moment $t_0^{(I+1)} = t_0^{(I)} + \Delta t$. The time step Δt is the duration between the activation of two consecutive sources. If the initial position of the moving heat source is $S_i^{(0)}$ and the velocity of the robot arm is v_i, then the position of heat source I is $S_i^{(I)} = S_i^{(0)} + v_i t_0^{(I)}$.

For the field $\tilde{T}$, a semi-infinite space, which is bounded by the top surface $\partial V_{\text{top}}^{(P)}$ of the part is considered. The field $\tilde{T}$ is then the temperature field due to all the heat sources in this semi-infinite space. For each discretised heat source, the Goldak double semi-ellipsoidal model is used. As shown in Fig. 3, the heat source profile consists of two semi-ellipsoids (the front semi-ellipsoid and the rear semi-ellipsoid). For any given source I, the corresponding analytical solution $\tilde{T}^{(I)}$ in a semi-infinite space reads

$$\tilde{T}(x_i, t)^{(I)} = \frac{B\Delta t}{D^{(I)}} \lambda_b^{(I)}(x_2) \lambda_c^{(I)}(x_3) [p_r^{(I)}(x_1) + p_f^{(I)}(x_1)], \tag{10}$$

where

$$
\begin{aligned}
B &= \frac{3\sqrt{3}PA}{\rho c_p \pi^{3/2}}, \\
D^{(I)} &= \sqrt{(3\eta^{(I)} + b^2)(3\eta^{(I)} + c^2)}, \\
\lambda_b^{(I)}(x_2) &= \exp(-\frac{3(S_2^{(I)} - x_2)^2}{3\eta + b^2}), \\
\lambda_c^{(I)}(x_3) &= \exp(-\frac{3(S_3^{(I)} - x_3)^2}{3\eta + c^2}), \\
p_r^{(I)}(x_1) &= \frac{f_r}{\sqrt{3\eta + a_r^2}} \exp(-\frac{3(S_1^{(I)} - x_1)^2}{3\eta + a_r^2})(1 - \mathrm{erf}(\frac{a_r(x_1 - S_1^{(I)})}{\sqrt{(3\eta + a_r^2)\eta\rho c_p}})), \\
p_f^{(I)}(x_1) &= \frac{f_f}{\sqrt{3\eta + a_f^2}} \exp(-\frac{3(S_1^{(I)} - x_1)^2}{3\eta + a_f^2})(1 - \mathrm{erf}(\frac{a_f(x_1 - S_1^{(I)})}{\sqrt{(3\eta + a_f^2)\eta\rho c_p}})), \\
\eta^{(I)} &= 4\alpha(t - t_0^{(I)}).
\end{aligned}
\tag{11}
$$

The detailed derivation of Eqs. (10) and (11) can be found in [27]. In Eq. (11), P is the power of the heat source. The non-dimensional coefficient A accounts for the absorption of the heat source energy and energy loss, such as due to radiation and phase transitions, which is not explicitly accounted for in the model. For a constant wire feed rate during the entire WAAM process, the parameter A can be assumed to be constant and is determined by calibrating the simulation temperature profiles with the experimental results. The parameter $\eta^{(I)}$ is to represent the time elapsed after the heat source I has been created. The term x_i denotes the coordinates of the point of interest and $S_i^{(I)}$ is the centre of the Goldak heat source with index I, as shown in Fig. 3. For the Goldak heat source that is schematically illustrated in Fig. 3, the semi-axes parallel to the x_1 axis of the front and the rear semi-ellipsoids are a_f and a_r, respectively. For both the front and the rear semi-ellipsoids, the semi-axes parallel to the x_2 and x_3 axes are b and c, respectively. The two factors f_f and f_r characterise the fractions of the heat deposited in the front and rear semi-ellipsoids, which satisfy $f_f + f_r = 2$. It can be seen in Eqs. (10) and (11) that the temperature $\tilde{T}(x_i, t)^{(I)}$ is related to the effective power PA, thermal properties k, ρ, c_p, semi-axes of the Goldak heat source (a_r, a_f, b, c), time term $\eta^{(I)}$, and the distance from the centre of the Goldak heat source to the point of interest, $(S_i^{(I)} - x_i)^2$ appearing in functions $\lambda_b^{(I)}, \lambda_c^{(I)}, p_r^{(I)}$ and $p_f^{(I)}$. A suggested way of estimating the semi-axes of the Goldak heat source (a_r, a_f, b, c) based on the metallographic profile of the welding bead can be found in [9]. Finally, the analytical solution of $\tilde{T}$ can be obtained by the summation of Eq. (10) using Eq. (5). The velocity v of the moving heat source is accounted for while determining the total number of the heat sources N as

$$
N = \frac{L}{v\Delta t}, \tag{12}
$$

where L is the length of the deposition path of interest.

For the complementary field $\hat{T}$, Eq. (6) is employed for a domain as shown in Fig. 2c. The BCs for $\hat{T}$ is expressed as

$$
k\frac{\partial \hat{T}}{\partial x_i}n_i = -k\frac{\partial \tilde{T}}{\partial x_i}n_i + h(T - T_\infty), \quad \text{on} \quad \partial V^{(B)} \quad \text{and} \quad \partial V^{(P)}. \tag{13}
$$

Recall that for the bottom surface $\partial V_{\text{bot}}^{(B)}$ of the baseplate, a greater value of convection coefficient h is assigned compared to the other boundary surfaces to simulate the cooling system underneath the baseplate. It should be noted that for the top surface $\partial V_{\text{top}}^{(P)}$ of the part, the gradient of $\tilde{T}$ along the normal direction of $\partial V_{\text{top}}^{(P)}$, i.e. $\partial\tilde{T}/\partial x_3$, is zero, which is a direct consequence of no flux BC on the boundary of the semi-infinite space considered for $\tilde{T}$.

Because the analytical field $\tilde{T}$ is intrinsically related to the distance from the heat source to the point of interest and the assumption that the semi-infinite space has homogeneous thermal properties k, ρ and c_p, the superposition principle requires the body V to have a convex shape. This means a straight line from any heat source to any point on

the boundary ∂V should be confined within body V, i.e. the straight line should not cross through any boundary. We refer to this as the "convexity" requirement.

It is important to note that in [20], Yang *et al.* utilised this semi-analytical approach to simulate the temperature histories of a LPBF process. A convex part was considered and the baseplate was not explicitly included in the analysis and thereby the "convexity" requirement was satisfied. However, in this paper, since the baseplate is included in the analysis, the "convexity" requirement cannot be strictly satisfied. It can be seen in Fig. 2b that for all the material points on the boundary surfaces of the part $V^{(P)}$ (such as point P1 shown in Fig. 2b) and some material points on the lateral surface $\partial V^{(B)}_{\text{lat}}$ and bottom surface $\partial V^{(B)}_{\text{bot}}$ of the baseplate, the "convexity" requirement is satisfied. On the other hand, for all the material points on the top surface $\partial V^{(B)}_{\text{top}}$ of the baseplate, the straight lines connecting these points (such as the condition for point P2 shown in Fig. 2b) to the heat sources cross through $\partial V^{(P)}_{\text{lat}}$. Therefore, directly applying Eq. (13) to enforce the BCs in $\hat{T}$ introduces some error.

For the material points on the lateral surface $\partial V^{(B)}_{\text{lat}}$ and bottom surface $\partial V^{(B)}_{\text{bot}}$ of the baseplate, the BCs as appeared in Eq. (13) can still be employed, if the baseplate $V^{(B)}$ is sufficiently large compared to the part $V^{(P)}$. This is because $\tilde{T}$ and its gradients decrease rapidly away from the heat sources. Therefore, for a large baseplate the distances between the heat sources and the points on the surfaces $\partial V^{(B)}_{\text{lat}}$ and $\partial V^{(B)}_{\text{bot}}$ are sufficiently large. Henceforth, the values of $\partial\tilde{T}/\partial x_i$ in Eq. (13) for surfaces $\partial V^{(B)}_{\text{lat}}$ and $\partial V^{(B)}_{\text{bot}}$ are very small. Therefore, even though some points on $\partial V^{(B)}_{\text{lat}}$ and $\partial V^{(B)}_{\text{bot}}$ violate the "convexity" requirement, it can be argued that the corresponding error introduced by using Eq. (13) is negligible.

The violation of the convexity requirement associated with the top surface of the baseplate $\partial V^{(B)}_{\text{top}}$ is more notable. However, since the $\tilde{T}$ field decreases away from the sources, directly using Eq. (13) would slightly underestimate the temperature. To compensate for this underestimation and to avoid making the proposed model too complex, the term $\partial\tilde{T}/\partial x_i$ in Eq. (13) is simply neglected for $\partial V^{(B)}_{\text{top}}$. The error introduced by this operation is expected to decrease rapidly with increasing built height, since the term $\partial\tilde{T}/\partial x_i$ would rapidly decrease with the increasing distance between the heat sources and the material points on $\partial V^{(B)}_{\text{top}}$.

Consequently, the BCs for solving $\hat{T}$ are given as

$$k\frac{\partial\hat{T}}{\partial x_i}n_i = -k\frac{\partial\tilde{T}}{\partial x_i}n_i + h(T - T_\infty), \quad \text{on} \quad \partial V^{(P)}, \quad \partial V^{(B)}_{\text{bot}} \quad \text{and} \quad \partial V^{(B)}_{\text{lat}}, \tag{14a}$$

$$k\frac{\partial\hat{T}}{\partial x_i}n_i = h(T - T_\infty), \quad \text{on} \quad \partial V^{(B)}_{\text{top}}. \tag{14b}$$

The closed form expression for $\partial\tilde{T}/\partial x_i$ can be attained by taking the derivative of Eq. (10) and is given in Appendix A. At the beginning of the simulation while building the first layer, the initial temperature T_{ini} is set to be the room temperature. After a layer is completed, the geometry of the part $V^{(P)}$ is updated hence the next solid layer is included in the problem domain. For a typical WAAM process, a cooling period succeeds the completion of each layer so that the part cools down to a sufficiently low temperature value. Typically a certain range of interlayer temperature is maintained by utilisation of a cooling system and adjusting the interlayer waiting time to avoid deleterious microstructural precipitations or phase transformations. The cooling period is also modelled by the proposed model. Since the influence of a point heat source on the temperature field decreases rapidly with time, the contributions of the heat sources generated for the processing of the previous layer are neglected for the subsequent layers. This is especially a justified assumption for the large scale part and the long cooling period. Consequently, before simulating the next layer, the heat sources of the previous layer are deleted from the simulation. The temperature field at the end of the cooling period is set to be the initial temperature of the system for the calculation performed for the next layer.

2.3. Mechanical model

Once the temperature history $T(x_i, t)$ of the part is obtained, the corresponding thermal strain $\varepsilon^{\text{th}}_{ij}$ can be calculated as

$$\varepsilon^{\text{th}}_{ij} = \delta_{ij}\int_{T_{\text{ref}}}^{T}\alpha_{\text{th}}(T)\mathrm{d}T, \tag{15}$$

where δ_{ij} is Kroneckers delta and T_{ref} is the reference temperature, which is taken as the room temperature. The thermal expansion coefficient is denoted as α_{th}, which is temperature dependent.

The total strain field ε_{ij} is expressed as

$$\varepsilon_{ij} = \varepsilon^e_{ij} + \varepsilon^p_{ij} + \varepsilon^{\text{th}}_{ij}, \tag{16}$$

where ε^e_{ij} and ε^p_{ij} are the elastic and plastic strain, respectively.

The elasto-plastic constitutive law is employed and geometrically linear kinematics is assumed. The von Mises yield criterion with isotropic linear hardening is used to model the plasticity, which is given by

$$f^{\text{yield}} = \sigma_{\text{VM}} - \sigma_Y(\varepsilon^p_e, T), \tag{17}$$

where σ_{VM} is the von Mises stress and ε^p_e is the equivalent plastic strain. The yield stress is denoted as σ_Y and the yielding occurs at $f^{\text{yield}} = 0$.

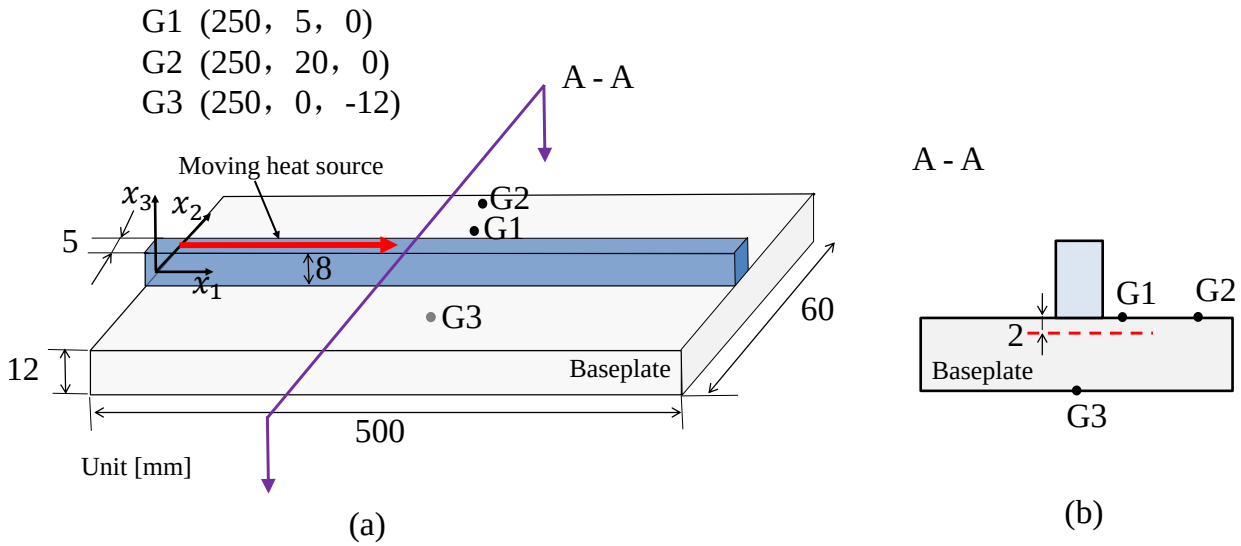

Figure 4: Schematic illustration of the problem. (a) The WAAM part built by Ding *et al.* [16] and the (b) 2D illustration of the cross-section A-A. The temperature evolution at selected points G1, G2 and G3 were measured by Ding *et al.* [16] using thermocouples. The residual stresses of the material points along the red dashed line were measured by Ding *et al.* [16] using neutron diffraction.

Table 1: Heat source parameters.

a_f (mm)	a_r (mm)	b (mm)	c (mm)	f_f (-)	f_r (-)
2	6	2.5	3	0.6	1.4

3. Problem Description

An experiment conducted by Ding *et al.* [16] is examined to assess the predictions of the proposed semi-analytical model. Therefore, our problem formulation follows this experiment. Ding *et al.* [16] deposited four layers of mild steel S355 with the layer thickness of 2 mm, as illustrated in Fig. 4. The power of the heat source was 2245 W while its speed was 8.33 mm/s. The wire feed rate was 10 m/min. The material was deposited along the centre line of the baseplate (see Fig. 4a) for building consecutive layers. The cooling time allowed after the deposition of each layer was

Table 2: Mechanical properties of mild steel S355 [9, 28] as a function of temperature, where E is the Young's modulus, ν is the Poisson's ratio, α_{th} is the thermal expansion coefficient, σ_Y is the yield strength.

T (°C)	E (GPa)	ν	α_{th}(°C^{-1})	$\sigma_Y(\varepsilon_e^p = 0)$ (MPa) deposited material	$\sigma_Y(\varepsilon_e^p = 0.01)$ (MPa) deposited material	$\sigma_Y(\varepsilon_e^p = 0)$ (MPa) baseplate	$\sigma_Y(\varepsilon_e^p = 0.01)$ (MPa) baseplate
20	206	0.29	1.2×10^{-5}	450	520	350	420
100	203	0.29	1.2×10^{-5}	450	520	330	400
200	201	0.295	1.2×10^{-5}	420	500	305	380
300	200	0.295	1.2×10^{-5}	390	450	270	350
400	165	0.3	1.2×10^{-5}	320	370	230	290
500	100	0.3	1.2×10^{-5}	260	300	180	230
600	60	0.32	1.2×10^{-5}	170	215	125	160
700	40	0.32	1.2×10^{-5}	60	100	60	100
800	30	0.35	1.2×10^{-5}	50	80	60	100
900	20	0.35	1.2×10^{-5}	50	50	60	60
1000	10	0.39	1.5×10^{-5}	50	50	60	60

400 s. The temperature histories of points G1, G2 and G3 (see in Fig. 4a and b) were measured using thermocouples. The residual stress components σ_{11}, σ_{22} and σ_{33} were measured using neutron diffraction along the red dashed line (see Fig. 4b), located at cross-section A-A, and 2 mm below the interface between the part and the baseplate.

Ding *et al*. [16] also utilised a non-linear transient thermo-mechanical FE model to simulate the above described WAAM process; see [9] for details. In this model [9, 16], Eq. (1) is used to calculate the temperature field. The Goldak heat source with a double semi-ellipsoidal power density distribution is employed. The material deposition is modelled using the *inactive* element approach. This implies the elements to be activated sequentially, following the motion of the heat source as the material is deposited. Finite elements that are not yet activated are excluded from the FE assembly and solution. The mechanical analysis was performed considering an elasto-plastic material as described in Section 2.3. The temperature dependences of both thermal and mechanical properties were accounted for.

For our proposed semi-analytical model recall that the Goldak heat source is also employed. The Goldak heat source parameters that are given by Ding *et al.* [16], tabulated in Table 1 are used for this purpose. The *inactive* element scheme is employed but in our scheme, the elements of an entire layer are simultaneously activated before the activation of the heat source. The convection coefficient h for the bottom surface of the baseplate is set to 300 W/m^{2}K which accounts for the cooling system, whereas it is assigned to be $h = 5.7$ W/m^{2}K for other boundaries following Ding *et al.* [9, 16]. The conductivity, density and specific heat are chosen as $k = 48.6$ W/mK, $\rho c_p = 3.9$ MJ/m^{3}K, respectively. These values correspond to 200 °C. The coefficient A is determined as $A = 0.78$. The values of the constant thermal properties and coefficient A are determined for model calibration based on a good agreement attained with the experiments after running a series of numerical trials. It is found that the coefficient A mainly affects the peak temperature values but has an insignificant effect on the cooling rates. Therefore, the numerical trials are first performed with a fixed value of coefficient A and varying the thermal properties to reproduce the experimentally attained cooling rates. After determining the thermal constants, the coefficient A is tuned to have the best match with the experimentally measured temperature profiles. Determination of the values of $k, \rho c_p$ and A is further elaborated in the next section (see also Fig. 8a)

The above given thermal properties are also assigned to the baseplate. The room temperature is taken as $T_\infty = 25$°C and the melting point of mild steel is $T_{\text{melt}} = 1500$ °C. Temperature dependent mechanical properties tabulated in Table 2 [28] are employed in the proposed mechanical model. In the experiment, both the part and the baseplate were comprised of grades of mild steel and have identical elastic modulus and Poisson's ratio. However, the part and baseplate differ in plastic response as can be seen from Table 2.

Ding *et al.* [16] used a so-called "cut-off" temperature of 1000 °C to avoid difficulties in numerical convergence. This means the upper limit of the temperature in the mechanical analysis is taken as the "cut-off" temperature and changes in the mechanical properties above the "cut-off" temperature are hence neglected. To make a fair comparison, in the present study a "cut-off" temperature of 1000 °C is also implemented.

First, the temporal convergence for the calculation of $\tilde{T}$ field is investigated. For that purpose, we consider a moving heat source on a very large baseplate, which can be considered as a semi-infinite medium. The temperature

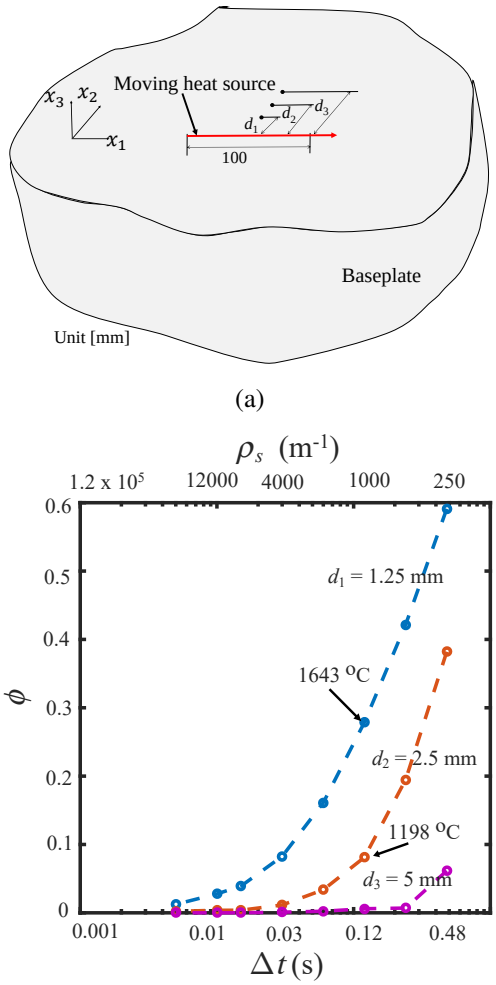

Figure 5: (a) A moving heat source on a very large baseplate assumed to be a semi-infinite space. The maximum temperatures $\tilde{T}_{\max}$ of three selected points with distances d_1, d_2 and d_3 to the moving heat source are investigated. (b) The parameter $\phi = |\tilde{T}_{\max} - \tilde{T}^{\text{ref}}_{\max}|/\tilde{T}^{\text{ref}}_{\max}$ is plotted as a function of the time increment Δt and the corresponding source density ρ_s. The reference value $\tilde{T}^{\text{ref}}_{\max}$ is calculated for $\Delta t = 0.001$ s. The horizontal axis is plotted in logarithmic scale. For the $\Delta t = 0.12$ s, the temperatures of the points with distance $d_1 = 1.25$ mm and $d_2 = 2.5$ mm are 1643 $^{\text{O}}$C and 1198 $^{\text{O}}$C, respectively.

field T can be then be directly determined by calculating $\tilde{T}$. We consider a moving heat source that moves for a total distance of 100 mm as shown in Fig. 5a. The maximum temperatures attained in this manner at three selected points, located at distances of $d_1 = 1.25$ mm, $d_2 = 2.5$ mm, and $d_3 = 5$ mm to the middle point of the heat source track, are calculated as a function of the time increment Δt. For the point with $d_1 = 1.25$ mm, the distance is almost half of the minimum semi-axis of the Goldak heat source ($a_f = 2$ mm), while for the point with $d_3 = 5$ mm, the distance is close to the maximum semi-axis of the Goldak heat source ($a_r = 6$ mm). The parameter $\phi = |\tilde{T}_{\max} - \tilde{T}^{\text{ref}}_{\max}|/\tilde{T}^{\text{ref}}_{\max}$ is defined to evaluate the temporal convergence of $\tilde{T}$ as function of Δt. The reference temperature $\tilde{T}^{\text{ref}}_{\max}$ is the maximum temperature of the point of interest, obtained with a very small time increment of $\Delta t = 0.001$ s. This time increment corresponds to a linear source density (number of heat sources per unit length, which is defined as $\rho_s = N/L = 1/v\Delta t$) of $\rho_s = 1.2 \times 10^5$ m^{-1}, for a velocity of 8.33 mm/s realised in the experiments conducted by Ding *et al.* [16].

The quantity ϕ at the selected points as a function of the time increment Δt as well as the source density ρ_s is

plotted in Fig. 5b. For the point with $d_3 = 5$ mm, $\tilde{T}$ quickly converges at approximately $\Delta t = 0.24$ s. For points with $d_2 = 2.5$ mm and $d_1 = 1.25$ mm, a smaller value of Δt is required. When $\Delta t = 0.12$ s, the quantity ϕ for the point with $d_2 = 2.5$ mm is less than 0.1, which indicates an error between the temperature $\tilde{T}$ and the reference value to be less than 10%. For the nearest point with $d_1 = 1.25$ mm, this discrepancy becomes 27%. Further investigation shows the corresponding temperature $\tilde{T}$ for $\Delta t = 0.12$ s at the point with $d_1 = 1.25$ mm is 1643 ^{o}C and $\tilde{T}$ calculated for the same time increment at the point with $d_2 = 2.5$ mm is 1198 ^{o}C. Recall that both of these values are higher than the "cut-off" temperature used in the proposed mechanical model. This means the use of time increment $\Delta t = 0.12$ s will not affect the accuracy of the mechanical analysis. Therefore, to guarantee considerable computational efficiency without sacrificing the accuracy when calculating the residual stresses and distortions, the maximum time increment of $\Delta t = 0.12$ s is employed in the remainder of the paper.

The proposed model is implemented using the commercial FE software ABAQUS. For the thermal model, linear heat transfer brick elements with 8 nodes (DC3D8 in ABAQUS) are chosen while for the thermo-mechanical model, the element type is the coupled displacement-temperature 8 nodded brick (C3D8RT in ABAQUS). The analytical field $\tilde{T}$ is calculated using the user subroutine *umatht* and the thermal BCs are applied using the subroutine $dflux$ to solve the complementary field $\hat{T}$. An automatic time-stepping scheme is used with a maximum time increment of $\Delta t = 0.12$ s to maintain a convergent source discretisation for $\tilde{T}$ calculation. During the cooling period, since the temperature values decay smoothly and no heat source is being created, a larger time increment Δt can be selected. After a series of numerical trials, it is found that convergence at $\Delta t = 10$ s is still reached. Hence, during the cooling period, the maximum time increment is set to be $\Delta t = 10$ s. The standard *coupled temp-displacement step* in ABAQUS is employed to conduct the one-way coupled thermo-mechanical calculation.

A thermal model with only half of the geometry by exploiting the symmetry in the problem is constructed, as shown in Fig. 6a. The deposited material has initially meshed with the mesh size of 5 mm $\times$ 0.3125 mm $\times$ 2 mm. The mesh size for the baseplate is 5 mm $\times$ 5 mm $\times$ 2 mm. We also use another coarser mesh for the deposited material, as shown in Fig. 6b. This is realised by increasing the mesh size of the part in the x_2 direction from 0.3125 mm to 1.25 mm. The results that are presented in the next section demonstrate that the temperature field obtained by this coarser mesh (Fig. 6b) is almost identical to that predicted by the fine mesh shown in Fig. 6a. This implies that the mesh density in the mesh shown in Fig. 6b is sufficient.

Finally, using the mesh shown in Fig. 6b, a thermo-mechanical model with half of the geometry is constructed, as shown in Fig. 6c. In the experiment performed by Ding *et al*. [16], the baseplate was fixed on a backing plate by clamps on the four corners and the middle points of the edges along the x_1 axis of the baseplate. Hence, corresponding nodes are fixed as shown in Fig. 6c. The backing plate is included in the model as a stationary rigid body. Hard contact is enforced between the contact surfaces of the backing plate and the baseplate. The backing plate prevents the movement of the baseplate in the negative x_3 direction but does not constrain its movement in the positive x_3 direction.

4. Results and Discussions

4.1. Thermal analysis

The temperature histories of points G1, G2 and G3 (see Fig. 4) are shown in Fig. 7. The blue dashed lines represent the experimental results. The red lines are the simulation results obtained from the semi-analytical thermal model with the fine mesh shown in Fig. 6a, whereas the black lines are the results obtained with the coarse mesh depicted in Fig. 6b. Good agreements with the experimental measurements are observed for both mesh densities. The predicted temperature for point G1 is slightly higher than the thermocouple measurement of Ding *et al* [16]. This discrepancy is expected to be mainly because points G1 and G2 are on the top surface of the baseplate, where the convexity is violated, and point G3 which is at the bottom surface of the baseplate, and the convexity is satisfied. The influence of non-convexity and the associated error for point G1 is more pronounced since the distance between point G1 and the moving heat source is smaller than that for point G2. For point G2, the influence of the non-convexity seems to be negligible, and the corresponding temperature prediction matches very well with the experimental data. Perfect agreement between the semi-analytical predictions and thermocouple measurements is observed for point G3 in Fig. 7c.

Fig. 8a shows how the coefficient A and thermal properties k and c_p influence the predicted temperature histories. The temperature history at point G2 while building the first layer is plotted in Fig. 8a for selected values of A, k and

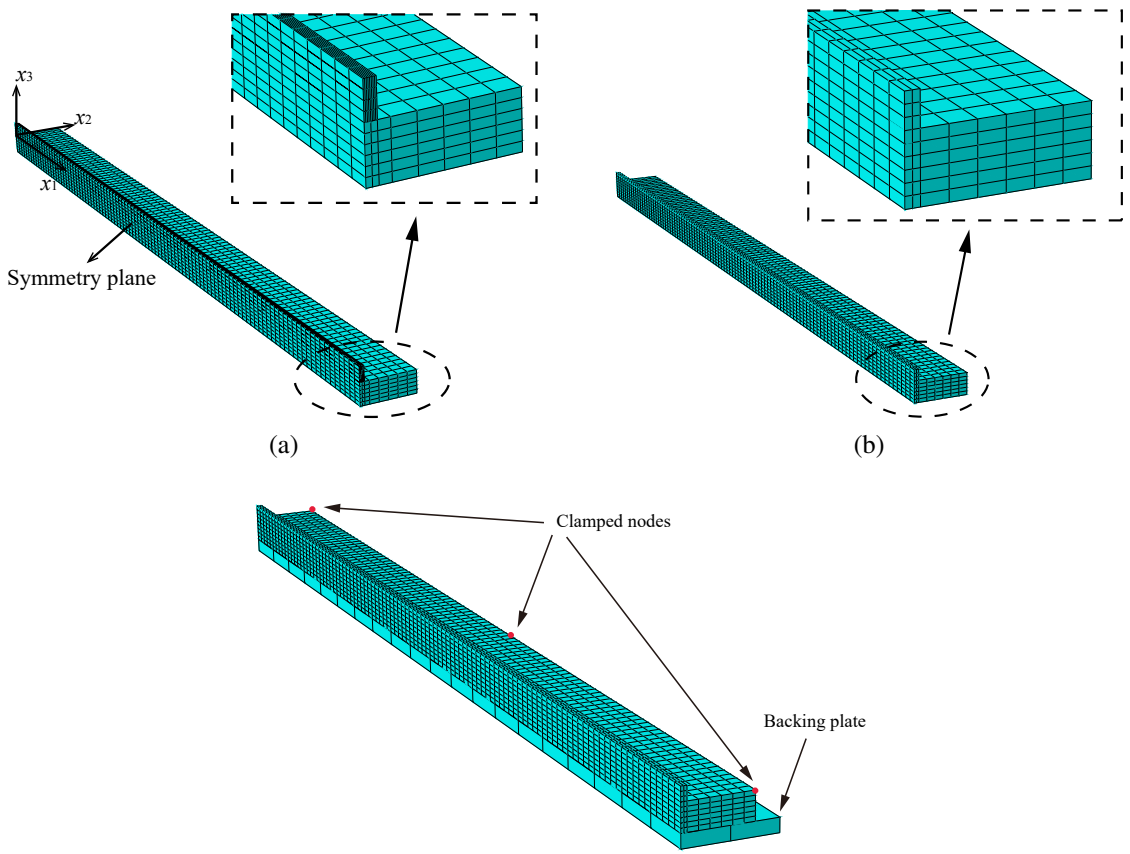

Figure 6: Finite element mesh depicted for half of the WAAM geometry with the (a) fine and (b) coarse mesh for the part. The baseplate is placed on a "backing plate", which is modelled as a stationary rigid body. Moreover, nodes on the baseplate are clamped.

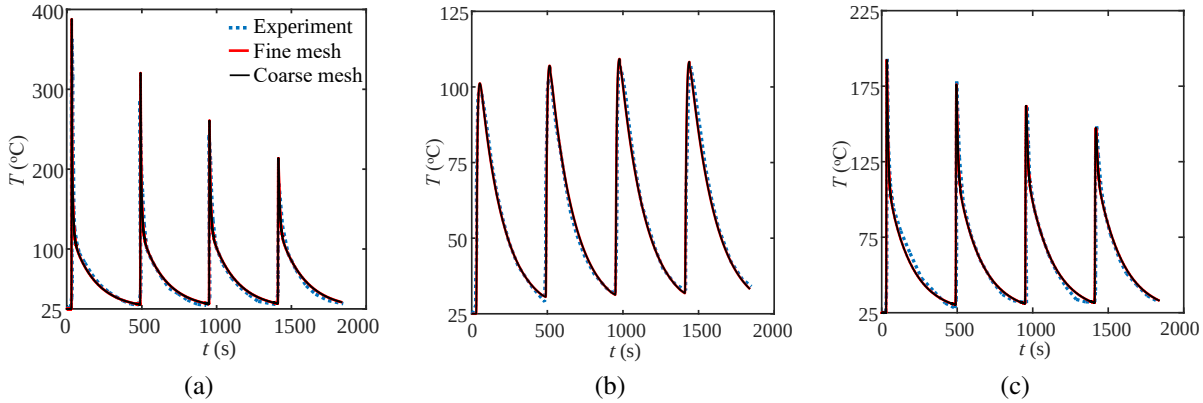

Figure 7: Temperature histories of points (a) G1, (b) G2 and (c) G3 that are shown in Fig. 4a. The blue dashed lines denote the experimental measurements reported by Ding *et al.* [16]. The red and black lines are the simulation results obtained with the fine (see Fig. 6a) and coarse (see Fig. 6b) meshes , respectively.

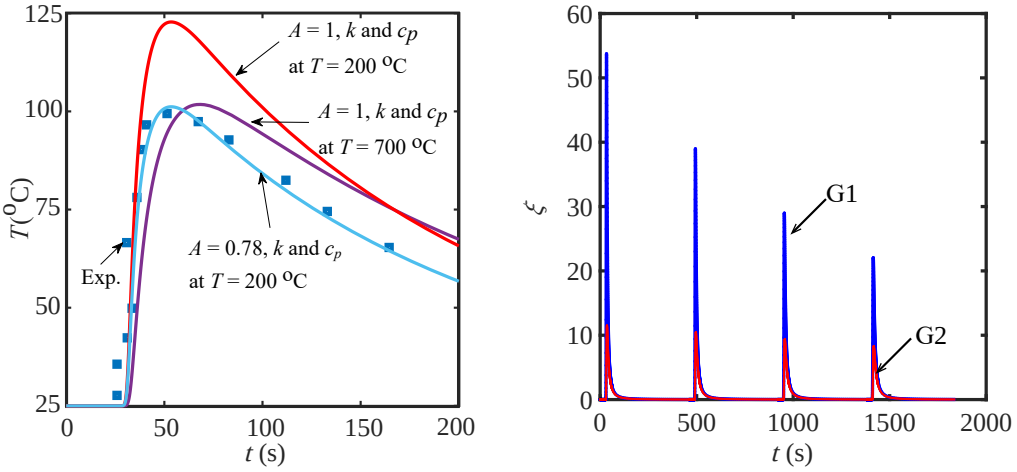

Figure 8: (a) Temperature history of point G2 while building the first layer for selected values of coefficient A and thermal properties at 200 °C and 700 °C. The blue dots are the experimental measurements reported by Ding *et al.* [16]. (b) The non-dimensional parameter ξ which indicates the intensity of heat flux at the top surface of the baseplate for points G1 and G2 as a function of time.

c_p. When the thermal properties corresponding to 700 °C are chosen, the cooling rate has a significant discrepancy with the experiment whereas the cooling rate observed for the temperature prediction using the thermal properties corresponding to 200 °C agrees well with the experiment. Note that the predicted peak temperature using the thermal properties at 700 °C is also not synchronised with the experimentally measured peak. When the thermal properties corresponding to 200 °C are chosen, it can be observed that both the temperature values and the heating and cooling rates perfectly match with the experiment upon choosing $A = 0.78$.

Recall that we neglect the term $\partial\tilde{T}/\partial x_i$ when enforcing the BCs on the top surface of the baseplate, $\partial V_{\text{top}}^{(B)}$, c.f. Eq. (14b). In order to quantify the degree of error associated with this assumption for the material points on the top surface $\partial V_{\text{top}}^{(B)}$ of the baseplate, we define a dimensionless quantity ξ as

$$\xi = \frac{k}{h(T_m - T_\infty)} \frac{\partial \tilde{T}}{\partial x_3}, \tag{18}$$

where $h = 5.7$ W/m^{2}K. In Fig. 8b, ξ is plotted as a function of time, for point G1 and point G2 . Since the only non-vanishing component of the unit surface normal is n_3 for $\partial V_{\text{top}}^{(B)}$, ξ does not depend on the x_1 and x_2 components of ∇T. It can be seen from Fig. 8b that distinct peaks of ξ are present for every layer of deposition. The ξ value peaks when the moving heat source is at $x_1 = 250$ mm, i.e. when it is the closest to the points of interest: G1 and G2. It can also be observed from Fig. 8b that the peak value for G1 is higher than that of G2 because G1 is closer to the track of the heat source. As time proceeds and the successive layers are deposited, the peak value of ξ decreases both for point G1 and point G2. This confirms the reasoning explained in Section 2.2 for the thermal BCs in Eq. (14b), regarding the diminishing influence of the gradient of $\tilde{T}$ with increasing part height. It is seen in Fig. 8b that even after four layers of deposition considered in the present study, high accuracy is anticipated (see Fig. 7) for the proposed model.

The temperature field $\tilde{T}$, i.e. the temperature due to the Goldak heat sources in a semi-infinite space, and the total temperature field $T = \tilde{T} + \hat{T}$ with actual BCs, are depicted in Fig. 9a and b, respectively. Fig. 9 is a snapshot during the deposition of the third layer. The temperature contour levels above the melting point are shown in white while the grey contour levels denote temperature values below 50°C. Next, the time evolution of $\tilde{T}$ and T of point G1 and point G2 are plotted in Fig. 10a and b, respectively. It can be observed both from Fig. 9 and Fig. 10 that consideration of the BCs is significant. The T is reasonably higher than $\tilde{T}$, and the cooling rate of $\tilde{T}$ is higher than that of T (see Fig. 10). Moreover, it can also be seen in Fig. 10a and b that the peak temperature of $\tilde{T}$ for building each layer decreases rapidly to a temperature close to the initial temperature 25 °C after about 150 s. This indicates that it is valid to assume the contributions of the heat sources generated for the processing of the previous layer can be neglected for the subsequent

layers.

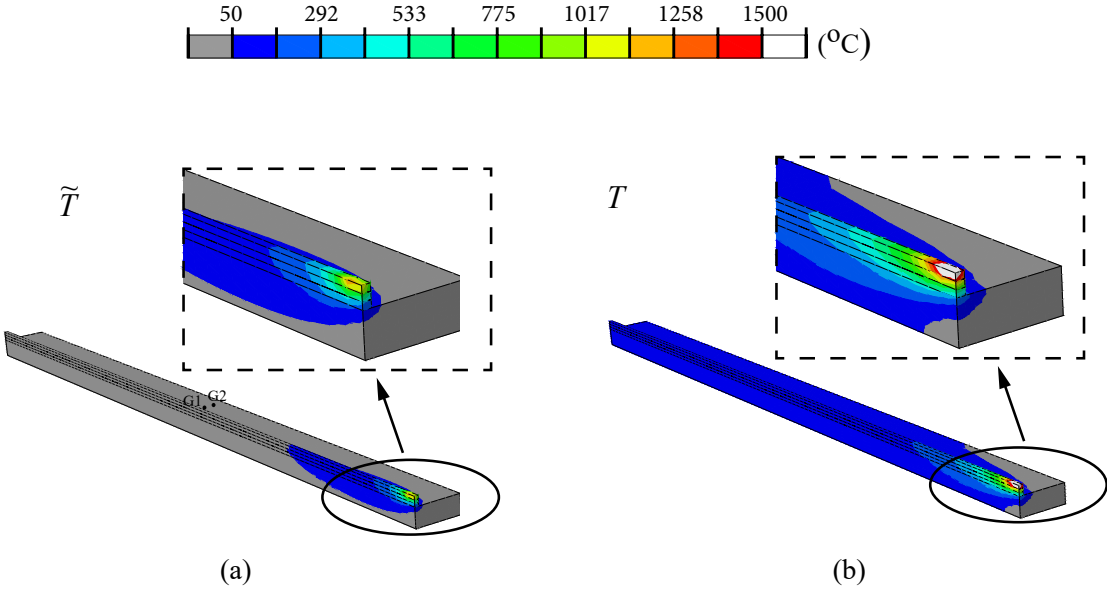

Figure 9: Snapshots of the (a) temperature field $\tilde{T}$ and (b) the total temperature field T at a time instant during the deposition of the third layer.

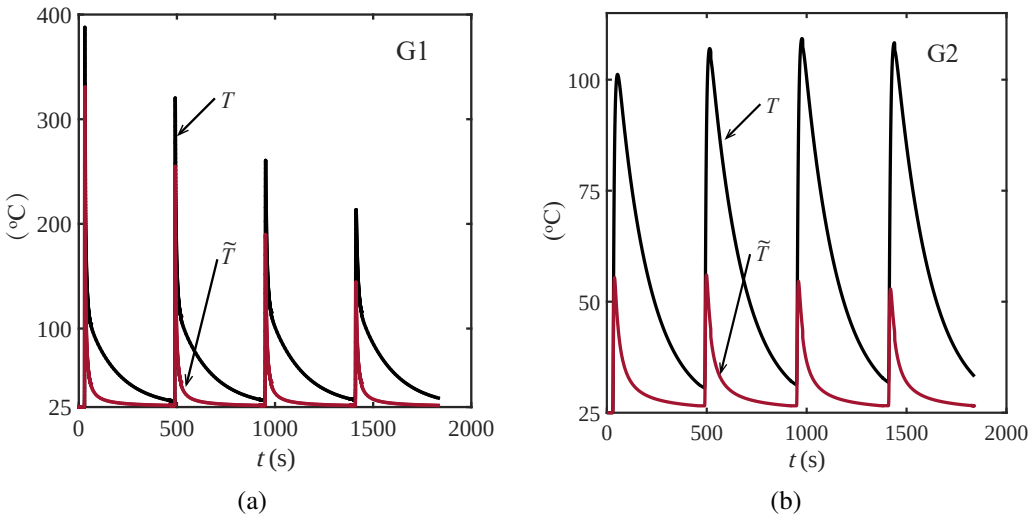

Figure 10: The temperature field $\tilde{T}$ and the total temperature T of points (a) G1 and (b) G2 as a function of time.

4.2. Mechanical analysis

It remains to predict the residual stresses and the deformations based on the semi-analytical thermal predictions. Thermal evolution of the body is used as an input to calculate the thermally induced displacement and stress fields. Recall that the temperature evolution is virtually identical for the two mesh sizes considered. Therefore, the coarse mesh shown in Fig. 6b is used for the thermo-mechanical calculations in the remainder of the paper. The temperature histories, mechanical BCs, elasto-plastic constitutive law and thermal expansion coefficient are factors that dictate the

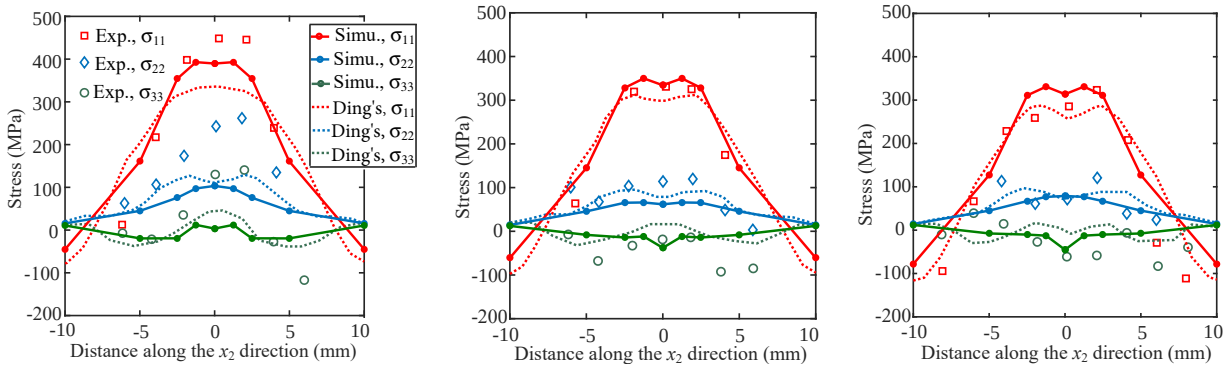

Figure 11: Residual stress components σ_{11}, σ_{22} and σ_{33} along the red dashed line indicated in Fig. 4b after building (a) a single layer, (b) two layers, and (c) three layers. The clamps are removed in both the experiments and simulations. The dashed lines are the results from the non-linear model developed by Ding *et al.* [16].

mechanical response of the body during WAAM. The accuracy of the proposed model will be evaluated by comparing model predictions with the experiments as well as the findings of the non-linear thermo-mechanical model reported by Ding *et al.* [16]. The experimentally measured residual stresses along the red dashed line which is 2 mm beneath the top surface of the baseplate (see Fig. 4b) after building various numbers of layers are compared with the corresponding simulation results in Fig. 11. The stress measurements were done upon removing the backing plate from the baseplate. To capture this in the simulations, the clamps on the three designated points (see Fig. 6c) are removed and the elements of the rigid stationary backing plate are deactivated. The results reported by Ding *et al.* [16] based on the non-linear thermo-mechanical model are also included in Fig. 11.

Table 3: The σ_{11} (MPa) at $x_2 = 0$ (see Fig. 11) for different layers.

	The proposed model	Ding's model [16]	Experiments [16]
Layer 1	389.7	336	448.6
Layer 2	334.2	298.9	330.6
Layer 3	313.6	256.9	285.7

Since the material is deposited along the x_1 axis, the part is mostly constrained against deforming along the x_1 direction. This is also evident from the experimental and simulation results given in Fig. 11. The normal stress along x_1 direction, i.e. σ_{11}, is more prominent than the normal stress components along the x_2 and x_3 directions. This is also in line with the typical stress profile observed in a long welding process [29]. Along the x_2 direction, between $x_2 = -2.5$ and $x_2 = 2.5$ mm, which corresponds to the width of the part, the stresses remain more or less constant. Beyond $x_2 = 2.5$ mm, the σ_{11} decreases rapidly. This can be rationalised by the decreasing temperature gradient along the x_2 direction away from the heat source located at $x_2 = 0$.

The stress evolution for a single layer of deposition is shown in Fig. 11a, and the predicted σ_{11} by the proposed semi-analytical model agrees well with the experiments. For stress components σ_{22} and σ_{33}, the peak values at $x_2 = 0$ obtained by the proposed model are lower than the experimentally measured values but agree well with the results from the model of Ding *et al.* [16]. In Fig. 11b and c, stress profiles in response to the deposition of the second and third layer are depicted, respectively. The simulation results by the proposed model agree very well with both the experiments and the simulation results obtained by Ding *et al.* [16]. As the height of the part increases the predictions become more in line with experimental measurements reminiscent of the trend seen for the thermal results given in Section 4.1. The peak values of σ_{11} at $x_2 = 0$ for different layers obtained by the proposed model, Ding's model [16] and the experiments are compared in Table 3. It can be calculated that the error between the predicted peak values by the proposed model and the experiment for the first layer is approximately 13%, and the same error for the second and third layers are both smaller than 10%.

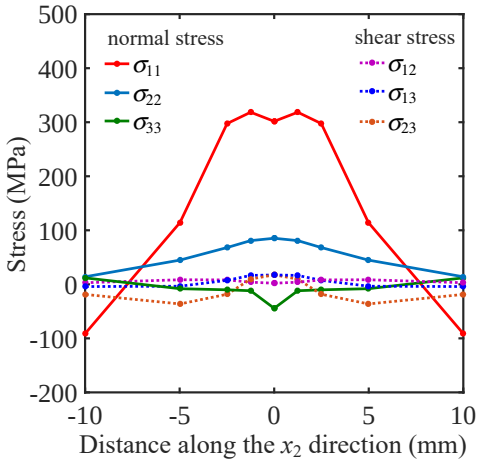

Figure 12: Residual stress components along the red dashed line indicated in Fig. 4b after building the fourth layer and removing the clamps. The solid lines are the normal stress components and the dashed lines are the shear stress components.

The six stress components along the red dashed line (Fig. 4b) after building the fourth layer are shown in Fig. 12. The results are obtained by removing the clamps and the backingplate (see Fig. 6). It can be seen that compared to the normal stress components σ_{11} and σ_{22}, the shear stress components are found to be insignificant since the thermal expansions and contractions generate only normal strains, c.f. Eq. (15).

Fig. 13 shows the σ_{11} distribution after completing the deposition of the fourth layer and subsequently removing

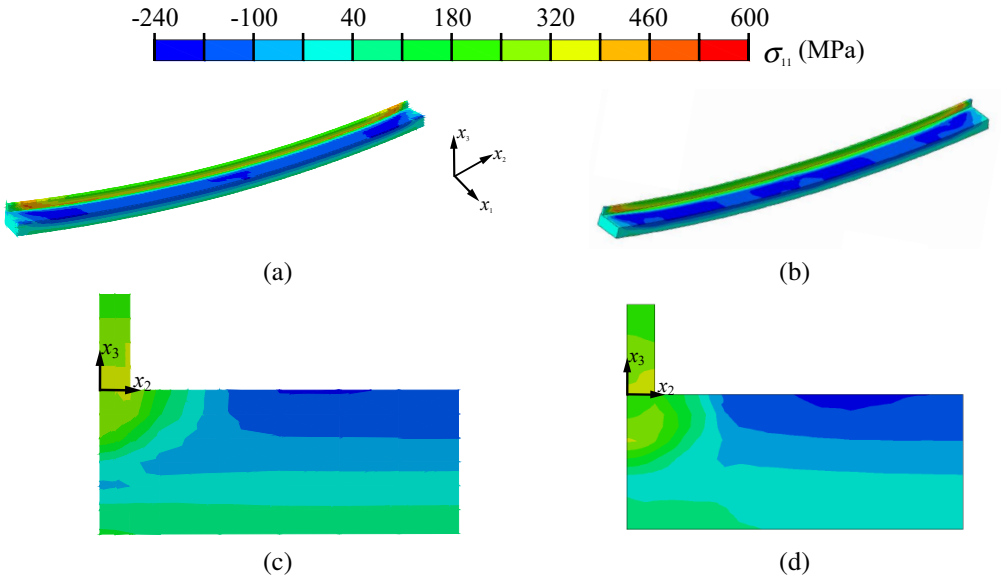

Figure 13: The distribution of σ_{11} after building the fourth layer and removing the clamps. The deformed shape of the WAAM sample, obtained by the (a) proposed model and (b) Ding's model *et al.* [9] (reproduced from [9] with permission). The stress distribution at the cross-section A-A (see Fig. 4) of the WAAM sample perpendicular to x_1 axis, obtained by (c) the proposed model and (d) Ding's model [9] (reproduced from [9] with permission). The displacements are amplified by a factor of five in (a) and (b) to improve visibility.

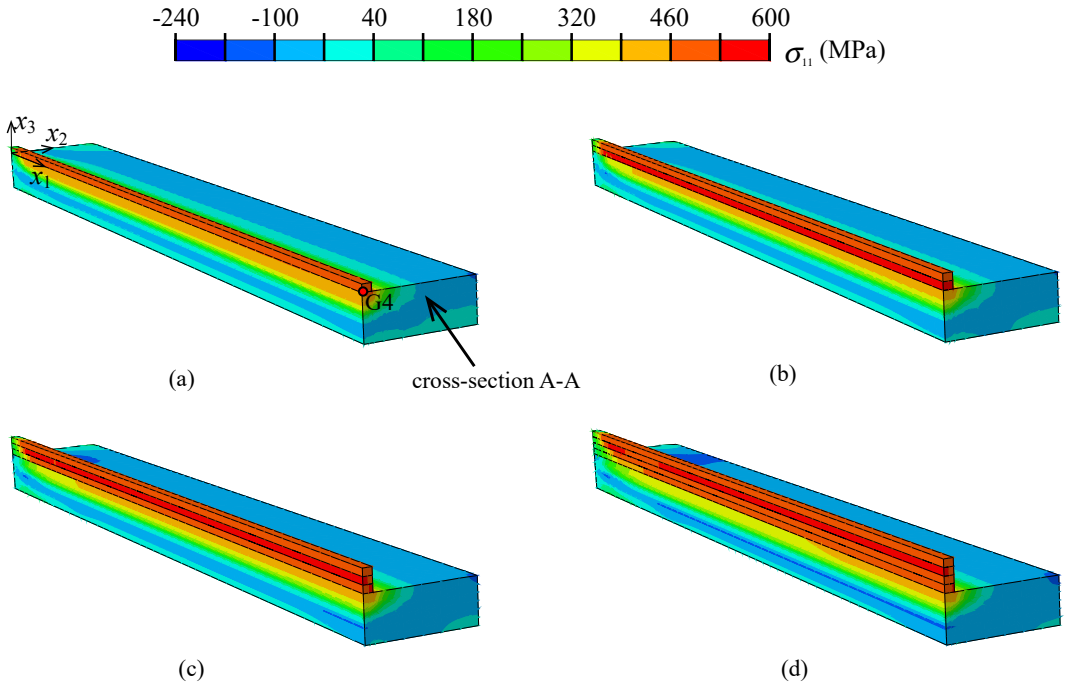

Figure 14: (a) The distribution of σ_{11} after building (a) a single layer, (b) two layers, (c) three layers and (d) four layers with the clamps in place. The backing plate is not shown to improve visibility.

the backing plate. Fig. 13a and c are the results obtained by the proposed model, and Fig. 13b and d are the simulation results from Ding [9]. In Fig. 13c and d, σ_{11} distribution for the cross-section A-A is illustrated. Similar stress distributions are attained with these two models. Consequently, the agreement of both models depicted in Fig. 11 along a line in the baseplate can be generalised for the whole domain of calculation. For the part, the stress σ_{11} decreases in the x_3 direction towards the top surface (see Fig. 13c and d). This is due to the stress relaxation facilitated by bending of the part as shown in Fig. 13a and b, upon detaching the baseplate from the rigid backing plate.

Snapshots of the stress distribution σ_{11} at different stages of the WAAM process, while the baseplate is still clamped to the backing plate, are shown from Fig. 14a to d. The part and the baseplate are shown as a cut through the cross-section A-A (see Fig. 4), i.e. only half of the length is shown. The location of the maximum σ_{11} is near the top surface of the part. For instance, after building the second layer, the maximum stress σ_{11} is observed in the first layer. This state of stress is partially relieved when the third layer is deposited. Similarly, after building the fourth layer the maximum σ_{11} is obtained at the location of the third layer. This is consistent with the simulation results reported in [30].

The evolution of σ_{11} and the magnitude of plastic strain $\bar{\varepsilon} = \sqrt{2\varepsilon_{ij}^p \varepsilon_{ij}^p/3}$ as a function of time is plotted in Fig. 15a, for point G4 on the baseplate. Point G4 is located on the cross-section A-A, and its location is illustrated in Fig. 15a as an inset. In Fig. 15a, one can observe the successive heating and cooling steps and the associated stress response. Once the heating of the first layer starts, point G4 endures a compressive σ_{11} since the thermal expansion due to temperature increase is constraint by the surrounding cooler regions, and thereby compressive stress is generated. Recall that as the temperature increases, yield strength decreases and plastic hardening is less pronounced. Therefore, this compressive stress induces significant plastic strain (see Fig. 15a). As the heat source moves away from point G4, local cooling at point G4 generates unloading and σ_{11} turns into tensile from compressive. Plastic strain magnitude decreases but the level of tensile stress fails to induce significant plastic strain at room temperature. During the rest of the cooling step, plastic strain magnitude remains constant and tensile σ_{11} slightly increases due to complete cooling of the part. Once the heating resumes, this time for the second layer, the same heating-cooling cycle creates the same stress cycle. However, as the number of layers increases the distance between the heat source and point G4 also

increases, and this leads to compressive σ_{11} not being able to induce plastic strain at point G4. Fig. 15b shows the contour levels of plastic strain magnitude $\bar{\varepsilon}$ distribution after completing the deposition of four layers. The first layer has the highest $\bar{\varepsilon}$ as it experiences the largest number of thermal cycles, indicating the first layer might be susceptible to plastic damage. The relatively larger $\bar{\varepsilon}$ at the corners of the baseplate is due to the clamps.

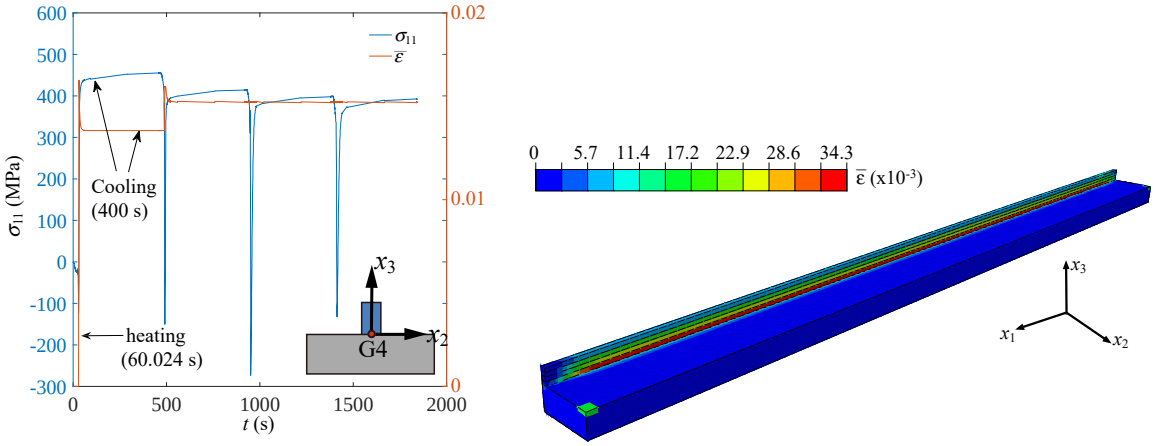

(a) (b)

Figure 15: (a) The evolution of stress σ_{11} and plastic strain amplitude $\bar{\varepsilon}$ with time for point G4 on the baseplate. The location of the point G4 is illustrated in the inset with the coordinates (250, 0, 0) mm. (b) The distribution of plastic strain amplitude $\bar{\varepsilon}$ after building the four layers.

The distribution of stress σ_{11} on the cross-section A-A, along the x_3 axis after completing the fourth layer is plotted in Fig. 16a. The results obtained with and without detaching the baseplate from the backing plate are both included in Fig. 16a. The results calculated by Ding [16] are also included. In Fig. 16a, $x_3 = 0$ indicates the interface between the part and the baseplate. It can be seen that the proposed model and the model by Ding [16] predict similar trends. There is a significant drop in stress σ_{11} after removing the baseplate from the backing plate due to the stress relaxation through bending. The stress jump at the interface between the part and the baseplate is the evidence of plastic deformation and the different plastic material models that are governing the part and the baseplate.

Fig. 16b shows the x_3 component of displacement u_3 along the length direction (x_1 direction) of the bottom surface of the baseplate. The simulation results obtained by the proposed model (the red solid line in Fig. 16b) agree perfectly well with the experimental measurements. It is also found that the predicted displacement profile is very sensitive to the BCs of the mechanical boundary value problem. When the bottom surface of the baseplate is fully constrained ($u_i = 0$) instead of modelling the backing plate which only constraints the movement of the baseplate in the negative x_3 direction, the corresponding bending indicated by the red dashed line in Fig. 16b is less.

4.3. Computational cost

The proposed model is implemented in ABAQUS for a single CPU with a processor speed of 2.80 GHz and with a memory of 16 GB RAM. The computational time of the proposed thermo-mechanical calculation described above is 3 hours and 15 minutes. The relatively low computational time required for the proposed model is mainly due to the coarse mesh size that can be used without loss of accuracy because the Goldak heat sources are accounted for analytically. This is attributed to the utilisation of the analytical field. Besides, at the start of adding a new layer, a very short duration of time ($t = 10^{-9}$ s in the present study) is allowed before simulating the real deposition process. This modification seems to be beneficial for the convergence of the mechanical boundary value problem. It is found that without this modification, the computational time increases to 8 hours.

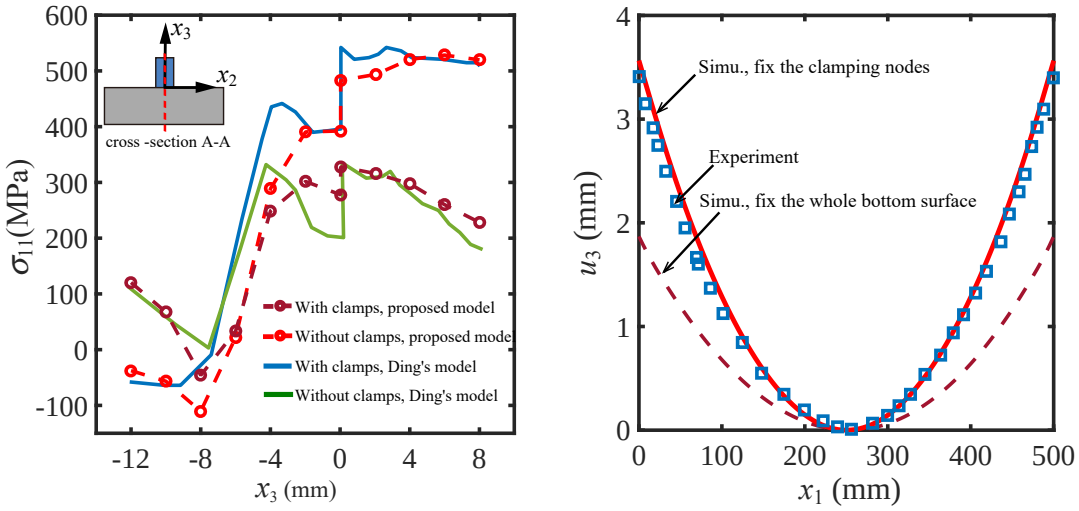

Figure 16: (a) The distribution of σ_{11} along the red dashed line illustrated in the inset. The $x_3 = 0$ denotes the interface between the part and the baseplate. (b) The x_3 component of displacement after building the fourth layer and removing the clamps.

5. Conclusions

A computationally efficient thermo-mechanical model for WAAM, based on the semi-analytical thermal approach is proposed. The accuracy of the proposed model is extensively examined by comparing the predicted thermal and mechanical results with the experimental measurements as well as the simulation results in the literature. It is found that considerable accuracy can be achieved by the proposed model in predicting the temperature history and stress evolution thereby predicting residual stresses and distortions.

For the studied modelling case, the simulation results show that the normal stress along the heat source motion is the dominating stress component, and the shear stresses are negligible. The maximum normal stress occurs near the top of the deposited layer. The distortions are very sensitive to the BCs, and more constraints of the baseplate may lead to smaller overall distortions. The proposed model is shown to be computationally inexpensive. This is primarily because the Goldak heat sources are accounted for by the analytical field $\tilde{T}$ and thereby the mesh size becomes independent of the heat source geometry. Furthermore, the proposed model is not necessarily limited to a long heat source moving path, for which a steady thermal state is reached. Instead, an arbitrary moving path of the heat source can be conveniently imported into the proposed model.

It should be noted that the non-linearity during the thermal simulation is not taken into account, and thus the value of thermal properties needs to be carefully determined by matching the predictions with experiments. Moreover, the proposed model is suitable only for materials whose residual stresses and distortions due to WAAM are not sensitive to the phase transitions and solid phase transformations.

Acknowledgements

Yabin Yang would like to acknowledge the financial support of the funding of Science and Technology on Plasma Dynamics Laboratory, Air Force Engineering University, Xian, China (Project No. 614220206021808).

Appendix A.

The partial derivative of $\tilde{T}^{(l)}$ with respect to x_1, x_2 and x_3 are expressed as

$$
\begin{aligned}
\frac{\partial \tilde{T}^{(I)}}{\partial x_1} &= \frac{B\Delta t}{D^{(I)}} \lambda_b^{(I)}(x_2)\lambda_c^{(I)}(x_3)[p_r'^{(I)}(x_1) + p_f'^{(I)}(x_1)], \\
\frac{\partial \tilde{T}^{(I)}}{\partial x_2} &= -\frac{6(x_2 - S_2^{(I)})}{3\eta^{(I)} + b^2}\tilde{T}^{(I)}, \\
\frac{\partial \tilde{T}^{(I)}}{\partial x_3} &= -\frac{6(x_3 - S_3^{(I)})}{3\eta^{(I)} + c^2}\tilde{T}^{(I)},
\end{aligned}
\tag{A.1}
$$

where

$$
\begin{aligned}
p_r'^{(I)}(x_1) &= \frac{f_r}{\sqrt{3\eta^{(I)} + a_r^2}}[-g_r^{(I)}(x_1)M_r'^{(I)}(x_1) - (1 - M_r^{(I)}(x_1)g_r'^{(I)}(x_1)], \\
p_f'^{(I)}(x_1) &= \frac{f_f}{\sqrt{3\eta^{(I)} + a_f^2}}[-g_f^{(I)}(x_1)M_f'^{(I)}(x_1) - (1 - M_f^{(I)}(x_1)g_f'^{(I)}(x_1)].
\end{aligned}
\tag{A.2}
$$

The $g_r(x_1), M_r(x_1), g_f(x_1), M_f(x_1)$ and the corresponding derivative $g_r'(x_1), M_r'(x_1), g_f'(x_1), M_f'(x_1)$ with respect to x_1 in Eq. (A.2) are directly computed as

$$
\begin{aligned}
g_r^{(I)}(x_1) &= \exp(-\frac{3(S_1^{(I)} - x_1)^2}{3\eta^{(I)} + a_r^2}), \\
g_r'^{(I)}(x_1) &= -\frac{6(x_1 - S_1^{(I)})}{3\eta^{(I)} + a_r^2} g_r^{(I)}(x_1), \\
M_r^{(I)}(x_1) &= \mathrm{erf}(\frac{a_r(x_1 - S_1^{(I)})}{\sqrt{(3\eta^{(I)} + a_r^2)\eta^{(I)}\rho c_p}}), \\
M_r'^{(I)}(x_1) &= \frac{2a_r}{\sqrt{(3\eta^{(I)} + a_r^2)\pi\eta^{(I)}\rho c_p}} \exp(-\frac{a_r^2(x_1 - S_1^{(I)})^2}{(3\eta^{(I)} + a_r^2)\eta^{(I)}\rho c_p}), \\
g_f^{(I)}(x_1) &= \exp(-\frac{3(S_1^{(I)} - x_1)^2}{3\eta^{(I)} + a_f^2}), \\
g_f'^{(I)}(x_1) &= -\frac{6(x_1 - S_1^{(I)})}{3\eta^{(I)} + a_f^2} g_f^{(I)}(x_1), \\
M_f^{(I)}(x_1) &= \mathrm{erf}(\frac{a_f(x_1 - S_1^{(I)})}{\sqrt{(3\eta^{(I)} + a_f^2)\eta^{(I)}\rho c_p}}), \\
M_f'^{(I)}(x_1) &= \frac{2a_f}{\sqrt{(3\eta^{(I)} + a_f^2)\pi\eta^{(I)}\rho c_p}} \exp(-\frac{a_f^2(x_1 - S_1^{(I)})^2}{(3\eta^{(I)} + a_f^2)\eta^{(I)}\rho c_p}).
\end{aligned}
\tag{A.3}
$$

Then the partial derivative of $\tilde{T}$ is given by

$$
\frac{\partial \tilde{T}}{\partial x_i} = \sum_{I=1}^{N} \frac{\partial \tilde{T}^{(I)}}{\partial x_i}. \tag{A.4}
$$

References

[1] B. Wu, Z. Pan, D. Ding, D. Cuiuri, H. Li, J. Xu, J. Norrish, A review of the wire arc additive manufacturing of metals: properties, defects and quality improvement, Journal of Manufacturing Processes 35 (2018) 127–139.

[2] D. Ding, Z. Pan, D. Cuiuri, H. Li, Wire-feed additive manufacturing of metal components: technologies, developments and future interests, The International Journal of Advanced Manufacturing Technology 81 (1-4) (2015) 465–481.

[3] B. A. Szost, S. Terzi, F. Martina, D. Boisselier, A. Prytuliak, T. Pirling, M. Hofmann, D. J. Jarvis, A comparative study of additive manufacturing techniques: Residual stress and microstructural analysis of clad and waam printed ti–6al–4v components, Materials & Design 89 (2016) 559–567.

[4] P. A. Colegrove, H. E. Coules, J. Fairman, F. Martina, T. Kashoob, H. Mamash, L. D. Cozzolino, Microstructure and residual stress improvement in wire and arc additively manufactured parts through high-pressure rolling, Journal of Materials Processing Technology 213 (10) (2013) 1782–1791.

[5] J. Hu, H.-L. Tsai, Heat and mass transfer in gas metal arc welding. part i: The arc, International journal of heat and mass transfer 50 (5-6) (2007) 833–846.

[6] H.-O. Zhang, F.-R. Kong, G.-L. Wang, L.-F. Zeng, Numerical simulation of multiphase transient field during plasma deposition manufacturing, Journal of applied physics 100 (12) (2006) 123522.

[7] L. Parry, I. Ashcroft, R. D. Wildman, Understanding the effect of laser scan strategy on residual stress in selective laser melting through thermo-mechanical simulation, Additive Manufacturing 12 (2016) 1–15.

[8] N. Hodge, R. Ferencz, J. Solberg, Implementation of a thermomechanical model for the simulation of selective laser melting, Computational Mechanics 54 (1) (2014) 33–51.

[9] J. Ding, Thermo-mechanical analysis of wire and arc additive manufacturing process.

[10] H. Zhao, G. Zhang, Z. Yin, L. Wu, A 3d dynamic analysis of thermal behavior during single-pass multi-layer weld-based rapid prototyping, Journal of Materials Processing Technology 211 (3) (2011) 488–495.

[11] X. Bai, H. Zhang, G. Wang, Improving prediction accuracy of thermal analysis for weld-based additive manufacturing by calibrating input parameters using ir imaging, The International Journal of Advanced Manufacturing Technology 69 (5-8) (2013) 1087–1095.

[12] V. Pavelic, Experimental and computed temperature histories in gas tungsten arc welding of thin plates, Welding Journal Research Supplement 48 (1969) 296–305.

[13] B. Andersson, Thermal stresses in a submerged-arc welded joint considering phase transformations, Journal of Engineering Materials and Technology, Trans. ASME 100 (1978) 356–362.

[14] E. Friedman, Thermomechanical analysis of the welding process using the finite element method, Journal Pressure Vessel Technology, Trans. ASME, 97 (1975) 206–213.

[15] J. Goldak, A. Chakravarti, M. Bibby, A new finite element model for welding heat sources, Metallurgical transactions B 15 (2) (1984) 299–305.

[16] J. Ding, P. Colegrove, J. Mehnen, S. Ganguly, P. S. Almeida, F. Wang, S. Williams, Thermo-mechanical analysis of wire and arc additive layer manufacturing process on large multi-layer parts, Computational Materials Science 50 (12) (2011) 3315–3322.

[17] M. M. Francois, A. Sun, W. E. King, N. J. Henson, D. Tourret, C. A. Bronkhorst, N. N. Carlson, C. K. Newman, T. Haut, J. Bakosi, et al., Modeling of additive manufacturing processes for metals: Challenges and opportunities, Current Opinion in Solid State and Materials Science 21 (LA-UR-16-24513).

[18] Y. Yang, F. van Keulen, C. Ayas, A computationally efficient thermal model for selective laser melting, Additive Manufacturing 31 (2020) 100955.

[19] D. Ding, Z. Pan, D. Cuiuri, H. Li, A practical path planning methodology for wire and arc additive manufacturing of thin-walled structures, Robotics and Computer-Integrated Manufacturing 34 (2015) 8–19.

[20] Y. Yang, M. Knol, F. van Keulen, C. Ayas, A semi-analytical thermal modelling approach for selective laser melting, Additive Manufacturing 21 (2018) 284–297.

[21] D. W. Mackowski, Conduction heat transfer: Notes for mech 7210, Mechanical Engineering Department, Auburn University.

[22] C. Ayas, J. Van Dommelen, V. Deshpande, Climb-enabled discrete dislocation plasticity, Journal of the Mechanics and Physics of Solids 62 (2014) 113–136.

[23] Y. Yang, X. Zhou, A volumetric heat source model for thermal modeling of additive manufacturing of metals, Metals 10 (11) (2020) 1406.

[24] T. Moran, D. Warner, N. Phan, Scan-by-scan part-scale thermal modelling for defect prediction in metal additive manufacturing, Additive Manufacturing 37 (2021) 101667.

[25] W. Hackenhaar, J. A. Mazzaferro, F. Montevecchi, G. Campatelli, An experimental-numerical study of active cooling in wire arc additive manufacturing, Journal of Manufacturing Processes 52 (2020) 58–65.

[26] D. Deng, Fem prediction of welding residual stress and distortion in carbon steel considering phase transformation effects, Materials & Design 30 (2) (2009) 359–366.

[27] V. D. Fachinotti, A. A. Anca, A. Cardona, Analytical solutions of the thermal field induced by moving double-ellipsoidal and double-elliptical heat sources in a semi-infinite body, International Journal for Numerical Methods in Biomedical Engineering 27 (4) (2011) 595–607.

[28] P. Michaleris, A. DeBiccari, Prediction of welding distortion, Welding Journal-Including Welding Research Supplement 76 (4) (1997) 172s.

[29] X. Y. Shan, M. J. Tan, N. P. Odowd, Developing a realistic fe analysis method for the welding of a net single-bead-on-plate test specimen, Journal of Materials Processing Technology 192 (2007) 497–503.

[30] T. Mukherjee, W. Zhang, T. DebRoy, An improved prediction of residual stresses and distortion in additive manufacturing, Computational Materials Science 126 (2017) 360–372.